



Recovering Quasi-Active Properties of Dendritic Neurons from Dual Potential Recordings

STEVEN J. COX AND BOYCE E. GRIFFITH

Department of Computational and Applied Mathematics, Rice University, 6100 Main St., Houston, TX 77005

cox@caam.rice.edu

griffith@cims.nyu.edu

Received September 6, 2000; Revised May 20, 2001; Accepted June 1, 2001

Action Editor: John Rinzel

Abstract. We develop the theory and accompanying algorithm for the recovery of a dendritic neuron's cytoplasmic resistivity, membrane capacitance, leakage conductance, and two maximal channel conductances from weighted averages of simultaneous recordings of somatic and dendritic potential following a somatic current stimulus. We test our results on two model systems with distinct, though prescribed, channel kinetics and branching patterns.

Keywords: identification, parameter estimation, moment methods, symbolic solution, Laplace transform

1. Introduction

We aim to show that the moment methods developed by Cox (1998) and Cox and Ji (2000) for the recovery of passive cable properties in branched dendrites may also be used to recover maximal conductances of channels with known kinetics. To our knowledge, this is the first direct attack on the recovery of such parameters. The previous attacks—most notably Rall et al. (1992), Surkis et al. (1998), Mainen and Sejnowski (1998), and Vanier and Bower (1999)—employ iterative means to land at a parameter set that produces a good fit between measured and computed potentials. In our approach, we offer a direct, constructive proof that the measured potentials indeed uniquely determine the sought after parameters. The argument is constructive in the sense that it immediately leads to a direct, noniterative recovery algorithm.

We develop our method in the context of dendritic neurons with two distinct types of ion channels. We recall the standard active model in Section 2. In Section 3, we linearize this model about the rest potential arriving at a linear, so-called quasi-active, model. We indi-

cate how one may symbolically compute the Laplace transform of the solution to the quasi-active system and arrive, in Section 4, at the precise formulation and solution of the inverse problem. Namely, we wish to infer the cytoplasmic resistivity, membrane capacitance, leakage conductance, and two maximal channel conductances from simultaneous measurement of the soma and distal potential following a somatic current stimulus. We note that Johnston et al. (1996) have developed the experimental apparatus by which such dual potential recordings may be obtained. In Sections 5 and 6, we demonstrate the validity and robustness of our solution procedure on synthetic data—first on a tree of squid giant axons sporting the standard potassium and sodium channels and second on a caricature of the laterodorsal tegmental neuron studied by Surkis et al. (1998).

2. The Active Model

We consider dendritic neurons with M edges and N branch points. In general, we shall use \mathcal{L} to denote the set of leaf indices. The branch index of the parent at

node k is p_k , while the branch indices of the two children are c_k^1 and c_k^2 . The radii and length of branch j are a_j and ℓ_j , respectively, each in cm . We suppose the membrane rest potential, E_r , to be known and denote by $v_j(x, t)$ (mV) the difference between actual membrane potential and rest membrane potential on the j th branch. The likewise adjusted ionic equilibrium potentials are denoted E_{Na} , E_K , and E_l . We shall assume uniform material properties throughout the tree—namely, its axoplasmic resistivity, R_i ($k\Omega cm$), membrane conductances, G_l , G_{Na} , G_K ($1/(k\Omega cm^2)$), and membrane capacitance, C_m ($\mu F/cm^2$). Balancing axial and membrane current produces

$$\frac{a_j}{2R_i} \partial_{xx} v_j = C_m \partial_t v_j + G_{Na} m_j^3 h_j (v_j - E_{Na}) + G_K n_j^4 (v_j - E_K) + G_l (v_j - E_l), \quad (1)$$

with the kinetics of the potassium and sodium channels governed by

$$\partial_t m_j = \alpha_m(v_j)(1 - m_j) - \beta_m(v_j)m_j \quad (2)$$

$$\partial_t h_j = \alpha_h(v_j)(1 - h_j) - \beta_h(v_j)h_j \quad (3)$$

$$\partial_t n_j = \alpha_n(v_j)(1 - n_j) - \beta_n(v_j)n_j. \quad (4)$$

If the neuron is initially at rest, then

$$v_j(x, 0) = 0 \quad (5)$$

$$m_j(x, 0) = \bar{m} \equiv \alpha_m(0)/(\alpha_m(0) + \beta_m(0)) \quad (6)$$

$$h_j(x, 0) = \bar{h} \equiv \alpha_h(0)/(\alpha_h(0) + \beta_h(0)) \quad (7)$$

$$n_j(x, 0) = \bar{n} \equiv \alpha_n(0)/(\alpha_n(0) + \beta_n(0)). \quad (8)$$

At each branch point, we enforce continuity of potential and conservation of current via

$$v_{p_k}(\ell_{p_k}, t) = v_{c_k^1}(0, t) = v_{c_k^2}(0, t), \quad (9)$$

$$a_{p_k}^2 \partial_x v_{p_k}(\ell_{p_k}, t) = a_{c_k^1}^2 \partial_x v_{c_k^1}(0, t) + a_{c_k^2}^2 \partial_x v_{c_k^2}(0, t). \quad (10)$$

Finally, assuming current stimulus at the soma and seals at the distal ends of the leaves, we arrive at

$$\partial_x v_1(0, t) = -\frac{R_i}{\pi a_1^2} i_0(t), \quad (11)$$

$$\partial_x v_j(\ell_j, t) = 0, \quad j \in \mathcal{L}. \quad (12)$$

We have ignored, in (11), the conductive and capacitive effects of the soma for reasons of exposition. Their absence will simplify our early analyses. We shall demonstrate in Section 6 exactly how they may be incorporated into the full model.

In each of the equations above, save (12), we note that j runs from 1 to M , the number of edges, while k runs from 1 to N , the number of branch points. Our assumption of two children per parent is merely one of convenience. There is nothing in what follows that does not extend immediately to trees of greater fecundity.

It is well known that the trivial solution to the above is unstable in the sense that if the stimulus, i_0 , exceeds a threshold (in amplitude and duration), then v_j does not tend to zero. Our interest here is in the subthreshold response and in particular what it may tell us about the neuron's electrical composition.

3. The Quasi-Active Approximation

In the subthreshold regime, one is tempted to linearize the Hodgkin-Huxley system about the rest state producing a quasi-active model. See Koch (1999, chap. 10) for the history of such models and their interpretations via phenomenological inductances. Starting from scratch, if the stimulus is $\varepsilon i_0(t)$ where i_0 is suprathreshold and ε is small, then the likely response is

$$v_j = \varepsilon \tilde{v}_j + O(\varepsilon^2)$$

$$m_j = \bar{m} + \varepsilon \tilde{m}_j + O(\varepsilon^2)$$

$$h_j = \bar{h} + \varepsilon \tilde{h}_j + O(\varepsilon^2)$$

$$n_j = \bar{n} + \varepsilon \tilde{n}_j + O(\varepsilon^2).$$

Substituting these into (1) to (4) and identifying of terms of order ε , we find

$$\begin{aligned} \frac{a_j}{2R_i} \partial_{xx} \tilde{v}_j &= C_m \partial_t \tilde{v}_j + G_{Na} \{ \bar{m}^3 \bar{h} \tilde{v}_j \\ &\quad - (3\bar{m}_j \bar{m}^2 \bar{h} + \bar{m}^3 \tilde{h}_j) E_{Na} \} \\ &\quad + G_K \{ \bar{n}^4 \tilde{v}_j - 4\bar{n}_j \bar{n}^3 E_K \} + G_l \tilde{v}_j \end{aligned} \quad (13)$$

$$\partial_t \tilde{m}_j = \sigma_m \tilde{v}_j - \tilde{m}_j / \tau_m \quad (14)$$

$$\partial_t \tilde{h}_j = \sigma_h \tilde{v}_j - \tilde{h}_j / \tau_h \quad (15)$$

$$\partial_t \tilde{n}_j = \sigma_n \tilde{v}_j - \tilde{n}_j / \tau_n, \quad (16)$$

where

$$\tau_g \equiv 1/(\alpha_g(0) + \beta_g(0)) \quad \text{and}$$

$$\sigma_g \equiv \alpha'_g(0)(1 - \bar{g}) - \beta'_g(0)\bar{g}, \quad g = m, h, n. \quad (17)$$

The initial conditions are accordingly

$$\tilde{v}_j(x, 0) = \tilde{m}_j(x, 0) = \tilde{h}_j(x, 0) = \tilde{n}_j(x, 0) = 0, \quad (18)$$

while the branch point and boundary conditions remain (9) to (12).

As (13) to (16) are simply a constant coefficient linear system of differential equations, we employ the Laplace transform. In the interest of denoting the Laplace transform of $f(t)$ by $\hat{f}(s)$ and not wishing for any symbol to wear two hats, we drop the tildes in what follows. Taking the Laplace transform of (14) to (16), we find

$$\hat{m}_j = \frac{\tau_m \sigma_m}{1 + s \tau_m} \hat{v}_j, \quad \hat{h}_j = \frac{\tau_h \sigma_h}{1 + s \tau_h} \hat{v}_j, \quad \hat{n}_j = \frac{\tau_n \sigma_n}{1 + s \tau_n} \hat{v}_j$$

and hence note that \hat{v}_j satisfies the ordinary differential equation

$$a_j \partial_{xx} \hat{v}_j(x, s) = \mu^2(s) \hat{v}_j(x, s), \quad (19)$$

where

$$\mu(s) = \sqrt{2R_i(C_m s + G(s))} \quad (20)$$

and

$$G(s) = G_l + \left(\bar{n}^4 + \frac{F_n}{1 + \tau_n s} \right) G_K + \left(\bar{m}^3 \bar{h} + \frac{F_h}{1 + \tau_h s} + \frac{F_m}{1 + \tau_m s} \right) G_{Na} \quad (21)$$

and

$$F_m = -3\tau_m \bar{m}^2 \bar{h} E_{Na} \sigma_m, \quad F_h = -\tau_h \bar{m}^3 E_{Na} \sigma_h, \quad (22)$$

and $F_n = -4\tau_n \bar{n}^3 E_K \sigma_n.$

It follows from (19) that \hat{v}_j is of the form

$$\hat{v}_j(x, s) = \gamma_j(s) \cosh(x\mu(s)/\sqrt{a_j}) + \dot{\gamma}_j(s) \sinh(x\mu(s)/\sqrt{a_j}), \quad (23)$$

where the γ_j and $\dot{\gamma}_j$ are determined by the transformed branch point and boundary conditions

$$\begin{aligned} \partial_x \hat{v}_1(0, s) &= -\frac{R_i}{\pi a_1^2} \hat{i}_0(s), \\ \partial_x \hat{v}_j(\ell_j, s) &= 0, \quad j \in \mathcal{L}, \\ \hat{v}_{p_k}(\ell_{p_k}, s) &= \hat{v}_{c_k^1}(0, s) = \hat{v}_{c_k^2}(0, s), \\ a_{p_k}^2 \partial_x \hat{v}_{p_k}(\ell_{p_k}, s) &= a_{c_k^1}^2 \partial_x \hat{v}_{c_k^1}(0, s) + a_{c_k^2}^2 \partial_x \hat{v}_{c_k^2}(0, s). \end{aligned}$$

For example, at the root, we find

$$\partial_x \hat{v}_1(0, s) = \dot{\gamma}_1 \frac{\mu(s)}{\sqrt{a_1}} = -\frac{R_i}{\pi a_1^2} \hat{i}_0(s).$$

This determines $\dot{\gamma}_1$, and so

$$\begin{aligned} \hat{v}_1(x, s) &= \gamma_1 \cosh(x\mu(s)/\sqrt{a_1}) \\ &\quad - \frac{R_i \hat{i}_0(s)}{\pi \mu(s) a_1^{3/2}} \sinh(x\mu(s)/\sqrt{a_1}). \end{aligned} \quad (24)$$

Similarly, at each leaf, the sealed end condition permits one to express $\dot{\gamma}_j$ in terms of γ_j . More precisely,

$$\begin{aligned} \hat{v}_j(x, s) &= \gamma_j \{ \cosh(x\mu(s)/\sqrt{a_j}) \\ &\quad - \tanh(\ell_j \mu(s)/\sqrt{a_j}) \sinh(x\mu(s)/\sqrt{a_j}) \}, \\ &\quad j \in \mathcal{L}. \end{aligned}$$

The remaining parameters are determined by the $3N$ node conditions,

$$a_{p_k}^{3/2} (\gamma_{p_k} \check{s}_{p_k} + \dot{\gamma}_{p_k} \check{c}_{p_k}) = a_{c_k^1}^{3/2} \dot{\gamma}_{c_k^1} + a_{c_k^2}^{3/2} \dot{\gamma}_{c_k^2} \quad (25)$$

$$\gamma_{p_k} \check{c}_{p_k} + \dot{\gamma}_{p_k} \check{s}_{p_k} = \gamma_{c_k^1} \quad (26)$$

$$\gamma_{c_k^1} = \gamma_{c_k^2}, \quad (27)$$

where

$$\begin{aligned} \check{s}_j &= \sinh(\ell_j \mu(s)/\sqrt{a_j}) \quad \text{and} \\ \check{c}_j &= \cosh(\ell_j \mu(s)/\sqrt{a_j}). \end{aligned}$$

As we have already solved for some of the $\dot{\gamma}_j$ this must be reflected in (25) to (27). For example, if a child of node k is a leaf (i.e., $c_k^i \in \mathcal{L}$), we replace

$$\dot{\gamma}_{c_k^i} \quad \text{with} \quad -\check{t}_{c_k^i} \gamma_{c_k^i} \quad \text{where} \quad \check{t}_j = \check{s}_j / \check{c}_j. \quad (28)$$

Similarly, when $k = 1$, in which case $p_1 = 1$, we find

$$\begin{aligned} a_1^{3/2} (\gamma_1 \check{s}_1 + \dot{\gamma}_1 \check{c}_1) &= a_2^{3/2} \dot{\gamma}_2 + a_3^{3/2} \dot{\gamma}_3 \\ \gamma_1 \check{c}_1 + \dot{\gamma}_1 \check{s}_1 &= \gamma_2 \\ \gamma_2 &= \gamma_3. \end{aligned}$$

Given the $\dot{\gamma}_1$ computed on route to (24), the first two of these become

$$a_1^{3/2} \gamma_1 \check{s}_1 - a_2^{3/2} \dot{\gamma}_2 - a_3^{3/2} \dot{\gamma}_3 = \frac{R_i \hat{i}_0}{\pi \mu} \check{c}_1 \quad (29)$$

$$\gamma_1 \check{c}_1 - \gamma_2 = \frac{R_i \hat{i}_0}{\pi \mu a_1^{3/2}} \check{s}_1. \quad (30)$$

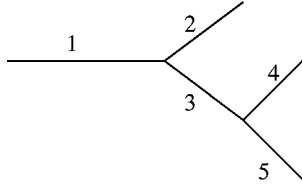


Figure 1. A simple dendrite.

As a concrete example, let us express the above for the branching pattern in Fig. 1.

In this case, the three matching conditions at each of the two nodes produce a linear system for the six unknowns $\Gamma = (\gamma_1 \gamma_2 \gamma_3 \check{\gamma}_3 \gamma_4 \gamma_5)$. Namely,

$$\begin{pmatrix} a_1^{3/2} \check{s}_1 & a_2^{3/2} \check{t}_2 & 0 & -a_3^{3/2} & 0 & 0 \\ \check{c}_1 & -1 & 0 & 0 & 0 & 0 \\ 0 & 1 & -1 & 0 & 0 & 0 \\ 0 & 0 & a_3^{3/2} \check{s}_3 & a_3^{3/2} \check{c}_3 & a_4^{3/2} \check{t}_4 & a_5^{3/2} \check{t}_5 \\ 0 & 0 & \check{c}_3 & \check{s}_3 & -1 & 0 \\ 0 & 0 & 0 & 0 & 1 & -1 \end{pmatrix} \times \begin{pmatrix} \gamma_1 \\ \gamma_2 \\ \gamma_3 \\ \check{\gamma}_3 \\ \gamma_4 \\ \gamma_5 \end{pmatrix} = \frac{R_i \hat{i}_0}{\pi \mu} \begin{pmatrix} \check{c}_1 \\ a_1^{-3/2} \check{s}_1 \\ 0 \\ 0 \\ 0 \\ 0 \end{pmatrix}. \quad (31)$$

It follows then that

$$\Gamma = \frac{R_i \hat{i}_0}{\pi \mu} y, \quad (32)$$

where y satisfies

$$A(\mu(s))y = b(\mu(s)) \quad (33)$$

and A and b are the matrix and right-hand-side vector appearing in (31). We note that it is a simple matter to automate the symbolic generation of A and b from purely morphological data.

Our main observation, however, is that this linear system, (33), may be solved symbolically for y as a function of the independent variable μ regardless of how μ itself may depend upon s . In other words, (33) comprises a natural splitting of the problem, and solution, into its purely *geometrical* (signified by $A(\mu)$ and $b(\mu)$) and *electrical* (signified by $\mu(s)$) features.

4. The Inverse Problem

The immediate upshot of this splitting is that the *transfer function* associated with a dendritic recording at point x on the j th branch,

$$\begin{aligned} T_j(x, s) &\equiv \frac{\hat{v}_1(0, s)}{\hat{v}_j(x, s)} \\ &= \frac{y_1(\mu(s))}{y_j(\mu(s)) \cosh(x\mu(s)/\sqrt{a_j}) + \check{y}_j(\mu(s)) \sinh(x\mu(s)/\sqrt{a_j})}, \end{aligned} \quad (34)$$

is *solely* a function of $\mu(s)$. To stress this point, we shall denote the right-hand side of (34) by $T_j(x, \mu(s))$ and so arrive at

$$T_j(x, s) = T_j(x, \mu(s)). \quad (35)$$

As the mapping $\mu \mapsto T_j(x, \mu)$ is known analytically, via symbolic means, and as $T_j(x, 0)$ is simply the ratio of the integrals of soma and distal potentials, we note that

$$\frac{\int_0^\infty v_1(0, t) dt}{\int_0^\infty v_j(x, t) dt} = T_j(x, \mu(0)) \quad (36)$$

is a single equation in the single unknown, $\mu(0)$. In the examples we have considered, we have found $\mu \mapsto T_j(x, \mu)$ to be monotone over the physiologically natural range of μ . This has permitted us to use bisection to solve (36) and thereby *uniquely* determine $\mu(0)$ from the two time integrals of the potential recordings. With

$$\mu(0) = \sqrt{2R_i G(0)} \quad (37)$$

determined, we now wish to show how to extract the five parameters of interest.

We begin with R_i . Recalling (32) we note that the *input impedance*,

$$z_1(s) \equiv \frac{\hat{v}_1(0, s)}{\hat{i}_0(s)} = \frac{R_i y_1(\mu(s))}{\pi \mu(s)}, \quad (38)$$

depends in a very simple manner on R_i . In particular, setting $s = 0$ in (38) produces the *explicit* representation,

$$R_i = \frac{\pi \mu(0)}{y_1(\mu(0))} \frac{\int_0^\infty v_1(0, t) dt}{\int_0^\infty i_0(t) dt}. \quad (39)$$

We obtain the remaining parameters, a bit less directly, via proper combinations of higher derivatives of μ at 0. These derivatives are obtained by repeated differentiation of (35). More precisely, via

$$\partial_s T_j(x, 0) = \partial_\mu T_j(x, \mu(0))\mu'(0) \quad (40)$$

$$\begin{aligned} \partial_s^2 T_j(x, 0) &= \partial_\mu^2 T_j(x, \mu(0))(\mu'(0))^2 \\ &\quad + \partial_\mu T_j(x, \mu(0))\mu''(0) \end{aligned} \quad (41)$$

$$\begin{aligned} \partial_s^3 T_j(x, 0) &= \partial_\mu^3 T_j(x, \mu(0))(\mu'(0))^3 \\ &\quad + 3\partial_\mu^2 T_j(x, \mu(0))\mu'(0)\mu''(0) \\ &\quad + \partial_\mu T_j(x, \mu(0))\mu'''(0). \end{aligned} \quad (42)$$

Each μ derivative of T_j at $\mu(0)$ is computed symbolically, while the s derivatives of T_j at 0 are compiled from moments of the two potential recordings. More precisely,

$$\partial_s T_j(x, 0) = \frac{M_0(v_1)M_1(v_j) - M_1(v_1)M_0(v_j)}{M_0^2(v_j)} \quad (43)$$

$$\begin{aligned} \partial_s^2 T_j(x, 0) &= (M_2(v_1)M_0^2(v_j) \\ &\quad - M_0(v_j)M_0(v_1)M_2(v_j) \\ &\quad - 2M_1(v_j)M_1(v_1)M_0(v_j) \\ &\quad + 2M_0(v_1)M_1^2(v_j)) / M_0^3(v_j) \end{aligned} \quad (44)$$

$$\begin{aligned} \partial_s^3 T_j(x, 0) &= (M_3(v_1)M_0^3(v_j) \\ &\quad - 6M_0(v_j)M_1(v_j)M_0(v_1)M_2(v_j) \\ &\quad + 3M_0^2(v_j)M_1(v_1)M_2(v_j) \\ &\quad + M_0^2(v_j)M_0(v_1)M_3(v_j) \\ &\quad + 3M_1(v_j)M_2(v_1)M_0^2(v_j) \\ &\quad - 6M_1^2(v_j)M_1(v_1)M_0(v_j) \\ &\quad + 6M_0(v_1)M_1^3(v_j)) / M_0^4(v_j), \end{aligned} \quad (45)$$

where

$$\begin{aligned} M_n(v_1) &\equiv \int_0^\infty t^n v_1(0, t) dt \quad \text{and} \\ M_n(v_j) &\equiv \int_0^\infty t^n v_j(x, t) dt \end{aligned} \quad (46)$$

are the n th moments of the respective potential readings. Agmon-Snir (1995) appears to have been the first to advocate the use of such moments in the classification and analysis of dendritic transients.

To recap, (40) to (45) permit the explicit expression of $\{\mu'(0), \mu''(0), \mu'''(0)\}$ in terms of moments of the measured potentials and symbolic solution of (33). It

remains then to show that these derivatives of μ indeed permit the extraction of the remaining parameters. To wit, recalling (20) and (21), we record

$$\mu'(0) = \frac{R_i(C_m + G'(0))}{\mu(0)}, \quad (47)$$

$$\mu''(0) = \frac{R_i G''(0)}{\mu(0)} - \frac{(\mu'(0))^2}{\mu(0)}, \quad (48)$$

$$\mu'''(0) = \frac{R_i G'''(0)}{\mu(0)} - 3 \frac{\mu'(0)\mu''(0)}{\mu(0)}, \quad (49)$$

and

$$\begin{aligned} G(0) &= G_l + (\bar{n}^4 + F_n)G_K \\ &\quad + (\bar{m}^3 \bar{h} + F_h + F_m)G_{Na}, \end{aligned} \quad (50)$$

$$G'(0) = -F_n \tau_n G_K - (F_h \tau_h + F_m \tau_m)G_{Na}, \quad (51)$$

$$G''(0) = 2F_n \tau_n^2 G_K + 2(F_h \tau_h^2 + F_m \tau_m^2)G_{Na}, \quad (52)$$

$$G'''(0) = -6F_n \tau_n^3 G_K - 6(F_h \tau_h^3 + F_m \tau_m^3)G_{Na}. \quad (53)$$

Given (48) and (49), we recognize (52) and (53) as a linear system for G_K and G_{Na} —namely,

$$\begin{aligned} &\begin{pmatrix} F_n \tau_n^2 & F_h \tau_h^2 + F_m \tau_m^2 \\ -3F_n \tau_n^3 & -3F_h \tau_h^3 - 3F_m \tau_m^3 \end{pmatrix} \begin{pmatrix} G_K \\ G_{Na} \end{pmatrix} \\ &= \frac{1}{2R_i} \begin{pmatrix} \mu(0)\mu''(0) + (\mu'(0))^2 \\ \mu(0)\mu'''(0) + 3\mu'(0)\mu''(0) \end{pmatrix}. \end{aligned} \quad (54)$$

This system is invertible as long as its determinant does not vanish—that is, as long as the value

$$F_m \tau_m^2 (\tau_n - \tau_m) + F_h \tau_h^2 (\tau_n - \tau_h)$$

is nonzero. Indeed, the determinant does not vanish so long as the kinetics of the gating variables are different. Having solved for G_{Na} and G_K , we can now solve for the value G_l . From (37) and (50) follows

$$G_l = \frac{\mu^2(0)}{2R_i} - (\bar{n}^4 + F_n)G_K - (\bar{m}^3 \bar{h} + F_h + F_m)G_{Na}. \quad (55)$$

Finally, we can solve for C_m by noticing from (47) that

$$C_m = \frac{\mu(0)\mu'(0)}{R_i} + F_n \tau_n G_K + (F_h \tau_h + F_m \tau_m)G_{Na}. \quad (56)$$

We recap the above in the following.

4.1. Recovery Algorithm

1. During a subthreshold current stimulus to the soma, record the soma and distal potentials, $v_1(0, \cdot)$ and $v_j(x, \cdot)$, and compute the nine moments, $M_0(i_0)$, $\{M_k(v_1)\}_{k=0}^3$, $\{M_k(v_j)\}_{k=0}^3$.
2. From the morphological data, symbolically construct and solve the linear system (33) for $y(\mu)$.
3. From y , construct the transfer function T_j , per right-hand side of (34).
4. Solve (36) via bisection for $\mu(0)$.
5. Evaluate R_i per (39).
6. Evaluate $\mu'(0)$, $\mu''(0)$ and $\mu'''(0)$ per (40) to (45).
7. Solve (54) for G_K and G_{Na} .
8. Evaluate G_l and C_m per (55) and (56).

Before applying this algorithm let us say a few words about its implementation. We have coded two distinct versions. The first is a hybrid Matlab-C routine that

- a. uses Matlab's Symbolic Toolbox to construct $y(\mu)$,
- b. from $y(\mu)$ automatically writes and compiles a C routine for finding $\mu(0)$,
- c. symbolically computes μ derivatives of T_j at $\mu(0)$.

The chief advantage of this code is that it is, essentially, a word-for-word implementation of the recovery algorithm. The chief disadvantage is the poor efficiency, regarding memory usage and cpu time, of current symbolic tools. For example, the wall clock times posted by a SUN workstation for execution of steps a, b, and c applied to the dendrite of Fig. 1 are 2, 4, and 173 seconds, respectively. The bulk of the time is spent in actually evaluating the derivatives of T_j at $\mu(0)$. Its third derivative, still in the context of Fig. 1, required 647 kbytes of memory. The timings and storage requirements increase so rapidly as one appends more branches to the tree that we turned to a more complicated pure C non-symbolic implementation. The complication arises in the differentiation of T_j with respect to μ . It follows from (34) that it suffices to differentiate y , the solution to (33), with respect to μ . We accomplish this by differentiating (33). More precisely, $\partial_\mu y(\mu(0))$ is the solution of the linear system

$$A(\mu(0))\partial_\mu y(\mu(0)) = \partial_\mu b(\mu(0)) - \partial_\mu A(\mu(0))y(\mu(0)).$$

The seemingly new functions, $\partial_\mu b$ and $\partial_\mu A$, may be generated at the same time as the original b and A

as they depend solely on morphology. In like fashion, higher derivatives of y may be derived from higher derivatives of A and b . By comparison with the symbolic code our straight numerical version required 19 wall clock seconds and occupied 2.5 Mbytes when applied to a dendrite with 127 branches.

Other implementation issues involve the choice of current stimulus and the optimal location for the dendritic recording. We shall experiment with different stimuli in the coming sections. Regarding positioning of the dendritic electrode we shall argue that the degree of fit—the quality of the recovery—increases with distance between the two recording sights. We can make this precise in the single fiber case. If x denotes the placement of the dendritic electrode, then the transfer function is

$$T_1(x, \mu(s)) = \frac{\cosh(\ell_1 \mu(s) / \sqrt{a_1})}{\cosh((\ell_1 - x) \mu(s) / \sqrt{a_1})}.$$

We recognize that $T_1(x, \cdot)$ is increasing for each x and note that (via (40) to (42)) the reliability of $\mu'(0)$, $\mu''(0)$ and $\mu'''(0)$ depend on $\partial_\mu T_1(x, \mu(0))$. The recovery is therefore less sensitive to noise the greater the value of $\partial_\mu T_1(x, \mu(0))$. It is a simple matter to show that $x \mapsto \partial_\mu T_1(x, \mu(0))$ is indeed an increasing function of x and so attains its maximum at the distal end $x = \ell_1$.

5. An Axon Tree

We consider the five-branch tree of Fig. 1 with branch lengths and radii

$$\begin{aligned} \ell_1 = 1, \quad \ell_2 = \ell_3 = 0.5, \quad \text{and} \quad \ell_4 = \ell_5 = 0.25 \text{ (cm)}, \\ a_1 = 0.0338, \quad a_2 = a_3 = 0.0138, \\ \text{and} \quad a_4 = a_5 = 0.0032 \text{ (cm)}, \end{aligned}$$

respectively. We assume the standard channel kinetics,

$$\begin{aligned} \alpha_m(v) &= \frac{25 - v}{10(e^{(25-v)/10} - 1)} \quad \text{and} \quad \beta_m(v) = 4e^{-v/18}, \\ \alpha_h(v) &= 0.07e^{-v/20} \quad \text{and} \quad \beta_h(v) = \frac{1}{e^{(30-v)/10} + 1}, \\ \alpha_n(v) &= \frac{10 - v}{100(e^{(10-v)/10} - 1)} \quad \text{and} \\ \beta_n(v) &= 0.125e^{-v/80}, \end{aligned}$$

reversal potentials

$$E_K = -12, \quad E_{Na} = 115, \quad E_l = 10.59892,$$

and parameters

$$R_i = 0.034, \quad C_m = 1, \quad G_K = 36, \\ G_{Na} = 120, \quad G_l = 0.3.$$

We shall use a fast, monophasic current stimulus

$$i_0(t) = I_0 t^2 e^{-10t} \quad (\mu A) \quad (57)$$

and a slow, multiphasic current stimulus

$$i_0(t) = I_0 t^2 e^{-5t} \sin(2\pi t) \quad (\mu A) \quad (58)$$

and measure the potential at the proximal end of branch 1 and the distal end of branch 5. Our measurements of $v_1(0, t)$ and $v_5(\ell_5, t)$ (see Figs. 2 and 3) result from solving the original active system, (1) to (10), via finite differences in space, $dx = 0.01$ (cm), and *fully implicit* backward Euler in time, $dt = 0.01$ (ms), with the parameters and kinetics as specified above.

With respect to (57), as an action potential is fired for I_0 in excess of 500, the quasi-active approximation is reasonable at $I_0 = 1$, and indeed the Recovery Algorithm performs extremely well in such case. In Table 1

Table 1. True and recovered parameters using (57).

	R_i	C_m	G_K	G_{Na}	G_l
True	0.034	1	36	120	0.3
$I_0 = 1$	0.0339	1.0029	36.0374	121.8159	0.3055
$I_0 = 10$	0.0339	0.9998	35.9045	120.5170	0.3034
$I_0 = 100$	0.0340	0.9655	34.4351	108.4737	0.2878
$I_0 = 200$	0.0342	0.9228	32.5510	95.6153	0.2736

Table 2. True and recovered parameters using (58).

	R_i	C_m	G_K	G_{Na}	G_l
True	0.034	1	36	120	0.3
$I_0 = 100$	0.0336	1.0575	38.3653	123.802	0.2828
$I_0 = 200$	0.0336	1.0952	39.9923	116.643	0.2352
$I_0 = 300$	0.0338	1.1218	41.1642	104.071	0.1747

we have charted its performance for increasing values of I_0 .

We note that as the stimulus is increased, the cell moves from quasi-active to active, and our recovery algorithm begins to break down, as expected. On adopting the multiphasic input we find instead the results shown in Table 2.

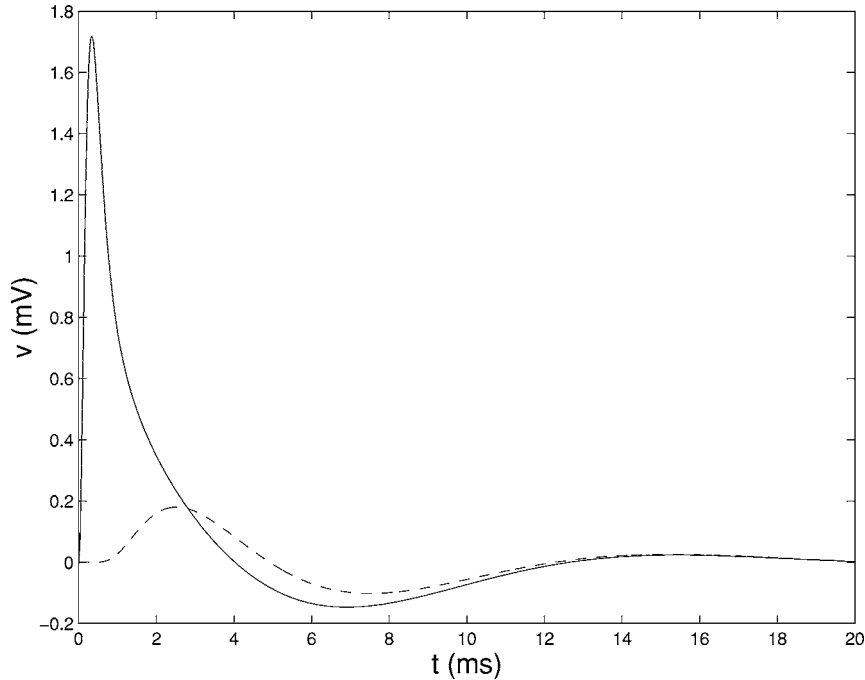


Figure 2. Computed soma (solid) and distal (dashed) potentials with $I_0 = 100$ in (57).

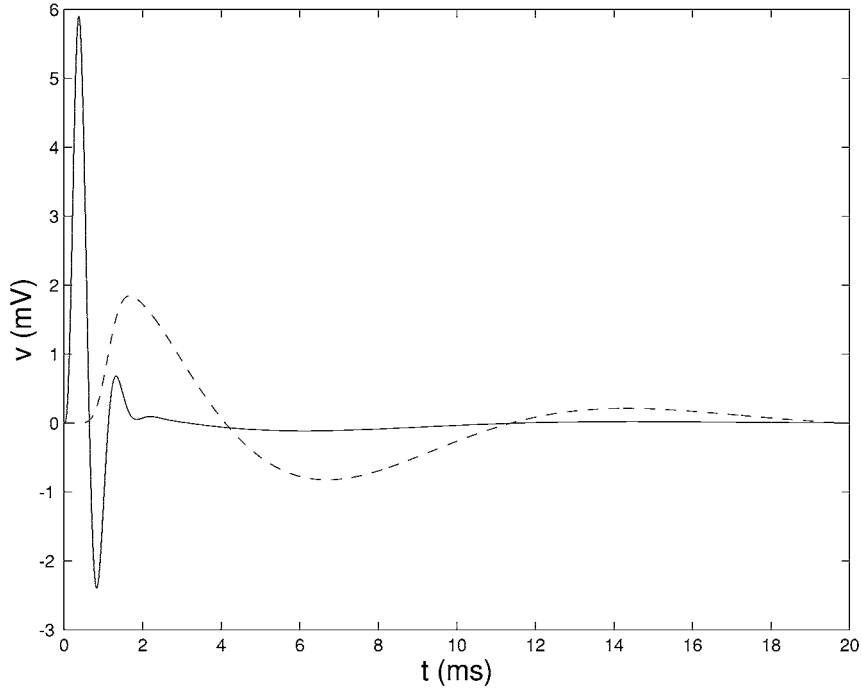


Figure 3. Soma (solid) and dendritic (dashed with $10\times$ magnification) potentials associated with (58) at $I_0 = 100$.

Again we see similar degradation in the recovery with increasing amplitude. We note however that while using (57) leads to underestimating C_m and G_K , just the opposite is true when using (58). This suggests that one may improve the estimates by averaging over a range of distinct current stimuli.

The success of the algorithm, at small stimuli, hinges on steps 4 and 7, as all other steps are mere evaluations. Regarding step 4 we have plotted in Fig. 4 the *exact* dependence of the transfer function, $T_j(x, \mu)$, upon μ . It is indeed monotone, and so our bisection routine has little trouble in returning the unique $\mu(0)$ (the μ corresponding to the \circ) given the ratio of the zeroth order moments of the two potential recordings. The error in the recovered $\mu(0)$ is essentially equal to the product of the error in the measured ratio and the reciprocal of the slope of $T_j(x, \cdot)$. As this slope is approximately 200 in the region of interest, we find that $\mu(0)$ is fairly insensitive to measurement error.

With respect to step 7, we note that

$$\begin{aligned} & \begin{pmatrix} F_n \tau_n^2 & F_h \tau_h^2 + F_m \tau_m^2 \\ -3F_n \tau_n^3 & -3F_h \tau_h^3 - 3F_m \tau_m^3 \end{pmatrix} \\ &= \begin{pmatrix} 0.7027 & 0.0431 \\ -11.5064 & -1.1050 \end{pmatrix} \end{aligned}$$

has a condition number (ratio of largest to smallest singular values) of 478, and hence the relative error in the recovered G_{Na} and G_K may be 478 times the relative error in the righthand side of (54). Such errors in μ and its derivatives at 0 stem from two independent sources: inaccurate estimates of branch radii and lengths and inaccurate measurement of the two potentials. The former produces errors in the $A(\mu)$ and $b(\mu)$ terms of (33) that in turn taint the computation of $T_j(x, \mu)$ and its derivatives with respect to μ . Errors in $v_1(0, t)$ and $v_j(x, t)$ of course produce errors in their moments and eventually taint the computation of $\mathcal{T}_j(x, s)$ and its derivatives with respect to s . We shall investigate the effects of noisy $v_1(0, t)$ and $v_j(x, t)$ in the next section.

6. A Laterodorsal Tegmental Neuron

For our second example, we attack a caricature of a laterodorsal tegmental (LDT) neuron previously studied by Surkis et al. (1998). Their model differs from the axon tree above in that their active elements included A and H type currents—that is,

$$\begin{aligned} \frac{a_j}{2R_i} \partial_{xx} v_j &= C_m \partial_t v_j + G_A m_j h_j (v_j - E_A) \\ &+ G_H n_j (v_j - E_H) + G_I (v_j - E_I), \quad (59) \end{aligned}$$

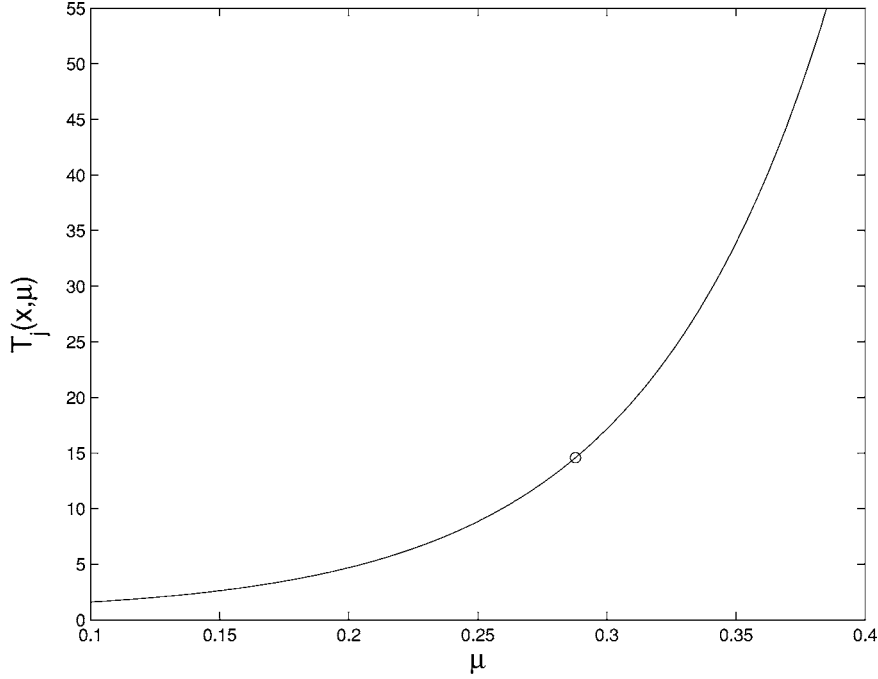


Figure 4. The analytically derived transfer function for the axon tree.

with kinetics

$$\begin{aligned}
 \alpha_m(v) &= \frac{1}{0.7(1 + e^{-(v+39-\Delta_A)/5.6})} \quad \text{and} \\
 \beta_m(v) &= \frac{1}{0.7} - \alpha_m(v), \\
 \alpha_h(v) &= \frac{1}{18(1 + e^{(v+57-\Delta_A)/4.8})} \quad \text{and} \\
 \beta_h(v) &= \frac{1}{18} - \alpha_h(v), \\
 \alpha_n(v) &= \frac{e^{-14.06 - 0.86v} + e^{-1.87 + 0.07v}}{1 + e^{(v+75-\Delta_H)/5.5}}, \\
 \beta_n(v) &= e^{-14.06 - 0.86v} + e^{-1.87 + 0.07v} - \alpha_n(v),
 \end{aligned} \tag{60}$$

where Δ_A and Δ_H are the shifts in the voltage at which half-maximum of the steady-state A -current and H -current activations are reached. In addition, they account for shunting at the soma via

$$\begin{aligned}
 \frac{\pi a_1^2}{R_i} \partial_x v_1(0, t) &= A_s \{ C_m \partial_t v_1(0, t) \\
 &+ G_{sh}(v_1(0, t) - E_{sh}) \\
 &+ G_A m_1 h_1 (v_1 - E_A) \\
 &+ G_H n_1 (v_1 - E_H) \} - i_0(t) \quad (61)
 \end{aligned}$$

rather than our naive (11). Here A_s denotes the surface area of the soma. Surkis et al. (1998) sought to recover R_i , C_m , G_{sh} , G_I , G_A , and G_H from measurement of $v_1(0, t)$ following a subthreshold somatic current stimulus via an indirect iterative method. More precisely, they adopted the Nelder-Mead simplex algorithm which, at each iteration, requires the costly solution of (59) to (61). We now show that these parameters may be determined directly from a few moments of the stimulus and somatic and dendritic potentials.

The quasi-active approximation of (59),

$$\begin{aligned}
 \frac{a_j}{2R_i} \partial_{xx} \tilde{v}_j &= C_m \partial_t \tilde{v}_j + G_A \{ \bar{m} \tilde{h} \tilde{v}_j - (\tilde{m}_j \bar{h} + \bar{m} \tilde{h}_j) E_A \} \\
 &+ G_H \{ \bar{n} \tilde{v}_j - \tilde{n}_j E_H \} + G_I \tilde{v}_j, \quad (62)
 \end{aligned}$$

produces (along the same lines as (21)) a generalized conductance of the form

$$\begin{aligned}
 G(s) &= G_I + \left(\bar{n} + \frac{F_n}{1 + \tau_n s} \right) G_H \\
 &+ \left(\bar{m} \bar{h} + \frac{F_h}{1 + \tau_h s} + \frac{F_m}{1 + \tau_m s} \right) G_A, \quad (63)
 \end{aligned}$$

where

$$\begin{aligned} F_m &= -\tau_m \bar{h} E_A \sigma_m, & F_h &= -\tau_h \bar{m} E_A \sigma_h, \\ \text{and } F_n &= -\tau_n E_H \sigma_n, \end{aligned} \quad (64)$$

and the τ , σ , and barred quantities are computed as in Sections 2 and 3. Recall (6) to (7) and (17), only now with respect to the kinetics in (60). This $G(s)$ also appears in the Laplace transform of the quasi-active approximation of the soma condition (61). Namely,

$$\begin{aligned} \frac{\pi a_1^2}{R_i} \partial_x \hat{v}_1(0, s) &= A_s(C_m s + G(s)) \\ &+ G_{sh} - G_l) \hat{v}_1(0, s) - \hat{i}_0(s). \end{aligned}$$

As \hat{v}_1 is still of the form (23), we find

$$\partial_x \hat{v}_1(0, s) = \gamma \frac{\mu(s)}{\sqrt{a_1}},$$

and so

$$\begin{aligned} \hat{\gamma}(s) &= \frac{R_i}{\pi a_1^{3/2} \mu(s)} (A_s(C_m s + G(s)) \\ &+ G_{sh} - G_l) \gamma_1(s) - \hat{i}_0(s). \end{aligned}$$

It follows then that

$$\begin{aligned} \hat{v}_1(x, s) &= \gamma_1(s) \left(\cosh(x\mu(s)/\sqrt{a_1}) \right. \\ &+ \frac{A_s(\mu^2(s)/2 + \zeta)}{\pi a_1^{3/2} \mu(s)} \sinh(x\mu(s)/\sqrt{a_1}) \left. \right) \\ &- \frac{R_i \hat{i}_0(s)}{\pi a_1^{3/2} \mu(s)} \sinh(x\mu(s)/\sqrt{a_1}), \end{aligned}$$

where

$$\zeta = R_i(G_{sh'} - G_l). \quad (65)$$

The upshot is that the first branch conditions, (29) to (30), become

$$\begin{aligned} a_1^{3/2} \gamma_1 \left(\check{s}_1 + \frac{A_s(\mu^2(s)/2 + \zeta)}{\pi a_1^{3/2} \mu(s)} \check{c}_1 \right) - a_2^{3/2} \check{\gamma}_2 - a_3^{3/2} \check{\gamma}_3 \\ = \frac{R_i \hat{i}_0}{\pi \mu} \check{c}_1 \end{aligned} \quad (66)$$

$$\gamma_1 \left(\check{c}_1 + \frac{A_s(\mu^2(s)/2 + \zeta)}{\pi a_1^{3/2} \mu(s)} \check{s}_1 \right) - \gamma_2 = \frac{R_i \hat{i}_0}{\pi \mu a_1^{3/2}} \check{s}_1. \quad (67)$$

and so the symbolic linear system, (33), now takes the form

$$A(\mu(s), \zeta)y = b(\mu(s)). \quad (68)$$

This shall require, of course, some modification of the Recovery Algorithm of Section 4. The modification however is minor, thanks to the fact that the associated transfer function is *independent* of the shunt parameter, ζ . (This can be seen by using the representation $A^{-1} = \mathcal{C}/\det(A)$, where \mathcal{C} is the transpose of the matrix of cofactors of A . Though ζ definitely appears in $\det(A)$, it is not hard to show, given the structure of A , that ζ does not appear in any of the cofactors associated with the upper left 2-by-2 subblock of A . As only the first two components of b are nonzero, it indeed suffices to consider only this subblock of A . As a result, each component of the solution, y , may be expressed as a numerator that is independent of ζ , divided by $\det(A)$. As each component has the same denominator, it follows that any ratio of linear combinations of these components (for example, our transfer function) will indeed be independent of ζ .) As such, it is only step 5 that needs attention. More precisely, the input impedance,

$$z_1(s) \equiv \frac{\hat{v}_1(0, s)}{\hat{i}_0(s)} = \frac{R_i \gamma_1(\mu(s), \zeta)}{\pi \mu(s)}, \quad (69)$$

indeed depends on both R_i and ζ . Its multiplicative dependence on R_i , however, suggests we look at the ratio of z_1 and its derivative—that is, at

$$\begin{aligned} \Phi(\zeta) &\equiv \frac{d}{ds} \Big|_{s=0} \log z_1(s) \\ &= \frac{\partial_\mu \gamma_1(\mu(0), \zeta) \mu'(0)}{\gamma_1(\mu(0), \zeta)} - \frac{\mu'(0)}{\mu(0)}. \end{aligned} \quad (70)$$

As $\mu'(0)$ may be computed directly from (40) and (43), we see that Φ indeed depends solely on ζ . The logarithmic derivative of z_1 at $s = 0$ is easily computed in terms of moments, so

$$\Phi(\zeta) = \frac{M_1(i_0)}{M_0(i_0)} - \frac{M_1(v_1)}{M_0(v_1)} \quad (71)$$

provides us with a single equation for the single unknown, ζ . After solving this for ζ , say by bisection, we may return to (69) and solve for

$$R_i = \frac{\pi \mu(0)}{\gamma_1(\mu(0), \zeta)} \frac{\int_0^\infty v_1(0, t) dt}{\int_0^\infty i_0(t) dt}. \quad (72)$$

One can then proceed as before to compute C_m , G_A , G_H , and G_I . With these in hand, one revisits (65) and finds

$$G_{sh} = G_I + \zeta/R_i. \quad (73)$$

We summarize the above in terms of the following.

6.1. LDT Recovery Algorithm

1. During a subthreshold current stimulus to the soma, record the soma and distal potentials, $v_1(0, \cdot)$ and $v_j(x, \cdot)$, and compute the two current moments, $M_0(i_0)$ and $M_1(i_0)$, and the eight voltage moments, $\{M_k(v_1)\}_{k=0}^3$, $\{M_k(v_j)\}_{k=0}^3$.
2. From the morphological data, symbolically construct and solve the linear system (33) for $y(\mu)$.
3. From y , construct the transfer function T_j , per right-hand side of (34).
4. Solve (36) via bisection for $\mu(0)$.
5. Evaluate $\mu'(0)$ with the help (40) and (43).
6. Solve (71) via bisection for ζ .
7. Evaluate R_i per (72).
8. Evaluate $\mu''(0)$ and $\mu'''(0)$ per (41) to (44) and (42) to (45).
9. Solve (54) for G_A and G_K .
10. Evaluate G_I and C_m per (55) and (56).
11. Evaluate G_{sh} per (73).

We have exercised this algorithm on the tree of Fig. 5 with branch lengths and radii

$$\begin{aligned} \ell_1 = 100, \quad \ell_2 = \ell_3 = 150, \quad \ell_4 = \ell_5 = \ell_7 = 250, \\ \text{and } \ell_6 = 300 \text{ } (\mu\text{m}), \\ a_1 = 3.38, \quad a_2 = a_3 = 1.38, \quad a_4 = a_5 = 0.88, \\ \text{and } a_6 = a_7 = 0.8 \text{ } (\mu\text{m}), \end{aligned}$$

respectively, a soma surface area of $A_s = 5026.5 \mu\text{m}^2$, reversal potentials

$$\begin{aligned} E_A = -97, \quad E_H = -40, \quad E_I = 0.954, \\ E_{sh} = 0.0959 \text{ (mV)}, \end{aligned}$$

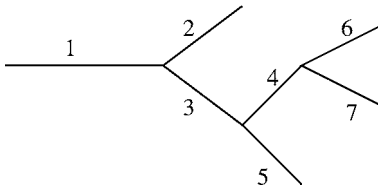


Figure 5. A crude LDT neuron.

and parameters

$$\begin{aligned} R_i = 0.4, \quad C_m = 1, \quad G_A = 0.15, \quad G_H = 0.04, \\ G_I = 0.02, \quad \text{and } G_{sh} = 0.19894, \end{aligned}$$

where, as above, R_i is in $\text{k}\Omega \text{ cm}$, C_m is in $\mu\text{F}/\text{cm}^2$, and the remaining conductances are in mS/cm^2 .

Using the monophasic stimulus, (57), we found that a gain of $I_0 = 0.1$ produced the 2 mV voltage swings observed by Surkis et al. (1998). We computed $v_1(0, t)$ and $v_7(\ell_7, t)$ by solving the full system, (59) to (61), via finite differences in space, $dx = 1 \mu\text{m}$, and fully implicit backward Euler in time, $dt = 0.01 \text{ ms}$, at differing channel shifts, Δ_A and Δ_H .

Using the data in Fig. 6, we visualize steps 4 and 6 of the LDT Recovery Algorithm in Fig. 7. Both graphs are monotone and steep and therefore deliver robust estimates of $\mu(0)$ and ζ .

Regarding step 9, we note, with $\Delta_A = 20$ and $\Delta_H = 40$, that the condition number of

$$\begin{aligned} \begin{pmatrix} F_n \tau_n^2 & F_h \tau_h^2 + F_m \tau_m^2 \\ -3F_n \tau_n^3 & -3F_h \tau_h^3 - 3F_m \tau_m^3 \end{pmatrix} \\ = \begin{pmatrix} -0.5257 & -2.8420 \\ 10.2333 & 153.4738 \end{pmatrix} \end{aligned} \quad (74)$$

is 458, and hence the recovery of G_A and G_H is quite sensitive to errors in μ and its derivatives at 0. This sensitivity may be evinced in a number of ways.

In what follows, we investigate the effect of working with realistic experimental measurements. We presume that random perturbations in the voltage recordings may be accounted for via averaging over multiple stimuli but that the resolution of the analog to digital converter is indeed finite. More precisely, in Table 3, we report the results of the LDT recovery algorithm when presented with only the first d digits of the measured $v_1(0, t)$ and $v_7(\ell_7, t)$.

Table 3. True and recovered LDT parameters drawn from measurements of varying precision. ($\Delta_A = 20$ and $\Delta_H = 40$)

	R_i	C_m	G_H	G_A	G_I	G_{sh}
True	0.4	1	0.04	0.15	0.02	0.19894
$d = 16$	0.40038	0.99675	0.04294	0.14984	0.02002	0.19916
$d = 6$	0.40038	0.9964	0.05061	0.14823	0.02009	0.19923
$d = 5$	0.40037	0.9947	0.08579	0.14056	0.02040	0.19954
$d = 4$	0.40027	0.9875	0.10302	0.24828	0.02186	0.20097

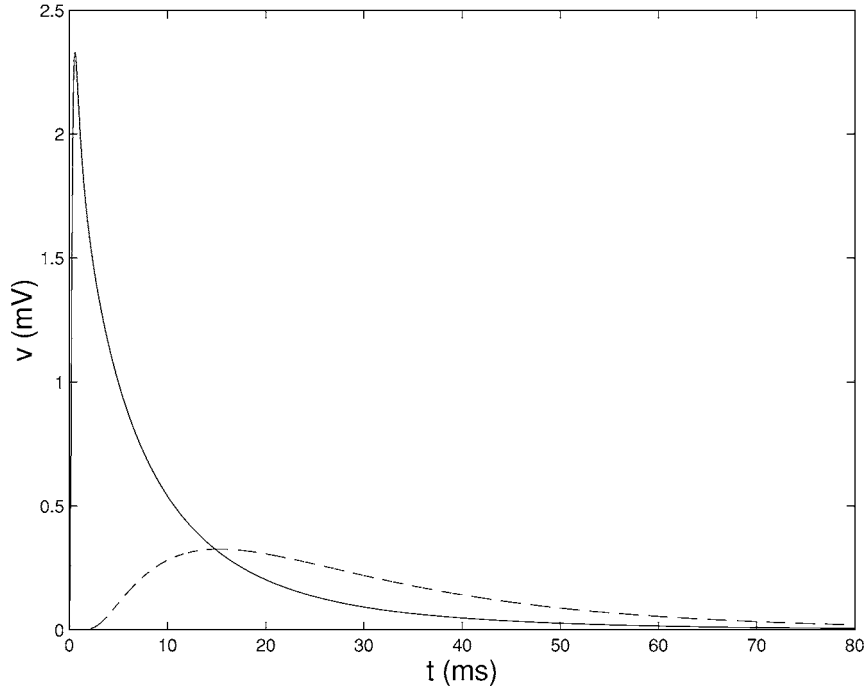


Figure 6. Computed soma (solid) and distal (dashed) LDT potentials with $I_0 = 0.1$, $\Delta_A = 20$ and $\Delta_H = 40$.

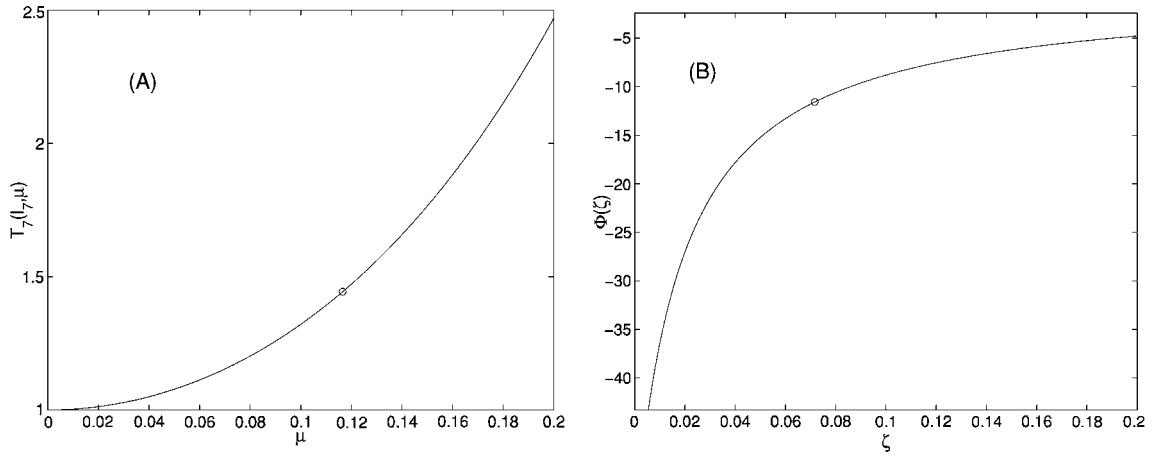


Figure 7. **A:** The LDT Transfer function and the computed $\mu(0)$. **B:** The graph of Φ , recall (70), and the computation of the ζ that satisfies (71).

We note the clear distinction in sensitivity between the passive and quasi-active parameters. The error in the latter is due to two sources: the poor conditioning of (74) and errors in μ and its derivatives stemming from errors in the moments due to rounding. We quantify this moment error in

$$\mathcal{E}_{d,n}(v) \equiv \frac{|M_n(v) - M_n(\text{round}(10^d v)10^{-d})|}{|M_n(v)|},$$

where round signifies “nearest integer.” If v is the soma potential of Fig. 6, we find the results shown in Table 4.

It is the 2.2% error in the third moment, when $d = 4$, coupled with the poor conditioning of (74), that produces the unacceptable error in the recovered channel conductances in the corresponding row of Table 3. There exist a number of possible remedies for this situation. First, retaining fewer than six digits is synonymous with neglecting the potential’s exponential tail.

Table 4. $\mathcal{E}_{d,n}(v_1(0, t))$. The relative error in the n th moment produced by retaining only d significant digits in the computed LDT soma potential.

	$n = 0$	$n = 1$	$n = 2$	$n = 3$
$d = 6$	4.2e-7	1.2e-5	1.2e-4	6.9e-4
$d = 5$	4.4e-6	9.8e-5	8.4e-4	4.1e-3
$d = 4$	4.2e-5	7.8e-4	5.5e-3	2.2e-2
$d = 3$	4.3e-4	6.0e-3	3.2e-2	10.0e-2

The absence of this tail becomes significant for the second and especially the third moments. One remedy then is to reattach the tail by fitting the existing decaying part of the measured potential to an exponential as, for example, when peeling the membrane time constant in passive models. A second remedy would be to use the value of C_m returned from, say, a passive recovery to remove our dependence on any third moments. More precisely, we note that, given R_i and C_m , Eqs. (47) and (48) comprise a 2-by-2 linear system for $G'(0)$ and $G''(0)$ (and hence for G_A and G_H) with no reliance on $\mu'''(0)$ and therefore no need for third moments. Finally, we note that the conditioning of (74) is very sensitive to the values the shifts, Δ_A

Table 5. True and recovered LDT parameters drawn from measurements of varying precision. ($\Delta_A = 15$ and $\Delta_H = 50$)

	R_i	C_m	G_H	G_A	G_l	G_{sh}
True	0.4	1	0.04	0.15	0.02	0.19894
$d = 16$	0.40038	0.99675	0.04294	0.14984	0.02002	0.19916
$d = 6$	0.40027	0.9964	0.04182	0.15138	0.02014	0.19927
$d = 5$	0.40026	0.9950	0.04666	0.13363	0.02040	0.19954
$d = 4$	0.40046	0.9882	0.06932	0.04530	0.02161	0.20077

and Δ_H . In particular, there is only a narrow band in the plane of (Δ_A, Δ_H) values for which (74) is fairly well-conditioned, as seen in Fig. 8.

For example, at $\Delta_A = 15$ and $\Delta_H = 50$, the condition number is only 62, an eightfold improvement over our previous choice. In Table 5, we report the findings of the LDT Recovery Algorithm when applied, as before, to increasingly rounded copies of the “true” potentials.

Although these new kinetics allow us to more accurately determine the active conductances, we still arrive at unacceptable estimates when faced with four or fewer digits. We now show how tail reattachment and prior knowledge of C_m lead to better estimates.

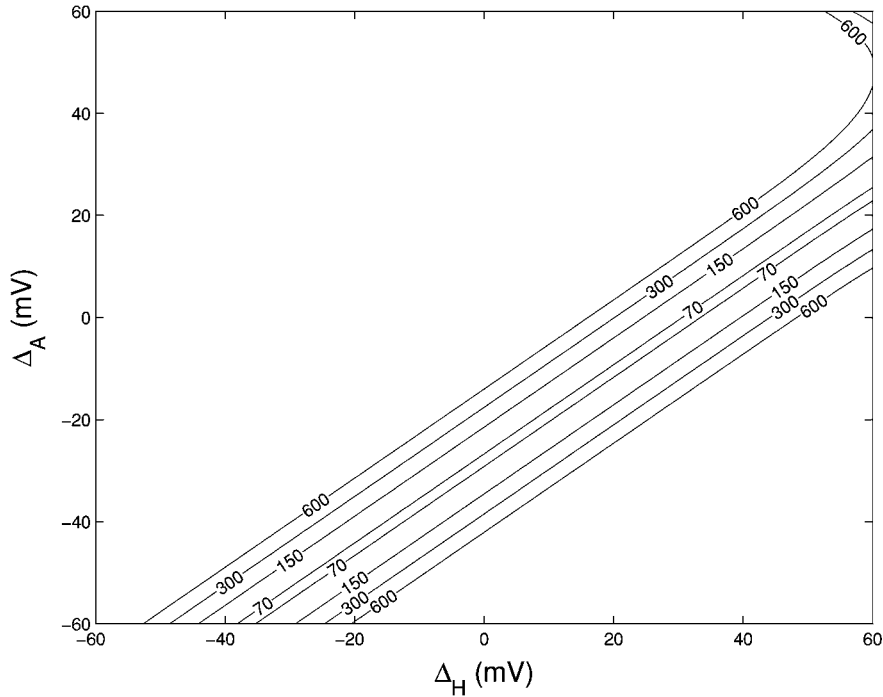


Figure 8. Contours of equal condition number of (74) as a function of Δ_A and Δ_H .

Analog to digital conversion of the biological potentials delivers piecewise constant approximations of the true signals. During intervals of rapid change this approximation is relatively benign. During long intervals of slow change, such as the early response of $v_7(\ell_7, t)$ and the late responses of both v_1 and v_7 , these errors accumulate when summed as parts of the required moments, (46).

To deal with this, we first smooth the digitized signal via simple averaging and then fit the early rise and late fall to exponentials that may be continued backward and forward in time. As an example, we “clean” the three-digit approximation of the $v_7(\ell_7, t)$ used in Table 5 above—that is,

$$\tilde{v}_7(\ell_7, t) = \text{round}(1000v_7(\ell_7, t))/1000.$$

Recall that, lacking biological potentials, the original v_7 is our stand-in for an uncorrupted dendritic recording. We depict in Fig. 9 the errors produced via such rounding and their partial alleviation via the aforementioned cleaning. Of course one could do better than Fig. 9B. The large early peak corresponds to our neglecting the rounding at the peak of $v_7(\ell_7, t)$. Given that our digitized samples stem from nonexperimental

Table 6. True and recovered LDT parameters drawn from cleaned measurements. ($\Delta_A = 15$ and $\Delta_H = 50$)

	R_i	C_m	G_H	G_A	G_I	G_{sh}
True	0.4	1	0.04	0.15	0.02	0.19894
$d = 4$	0.40046	0.9889	0.03061	0.19698	0.01954	0.19869

Table 7. True and recovered LDT parameters drawn from cleaned measurements but presuming $C_m = 1$. ($\Delta_A = 15$ and $\Delta_H = 50$)

	R_i	C_m	G_H	G_A	G_I	G_{sh}
True	0.4	1	0.04	0.15	0.02	0.19894
$d = 4$	0.40046	1.0000	0.03185	0.16138	0.01951	0.19868

synthetic measurement, we hesitate to process it any further. With respect to Table 5, when this cleaning procedure is applied, the $d = 4$ row becomes the results shown in Table 6.

This is a significant improvement. In Table 7 we contrast the $d = 4$ row of Table 5 with the improvement that comes from assuming prior (accurate) knowledge of C_m . Recall that in this case third moments are not required and so rounding may not play such a big role.

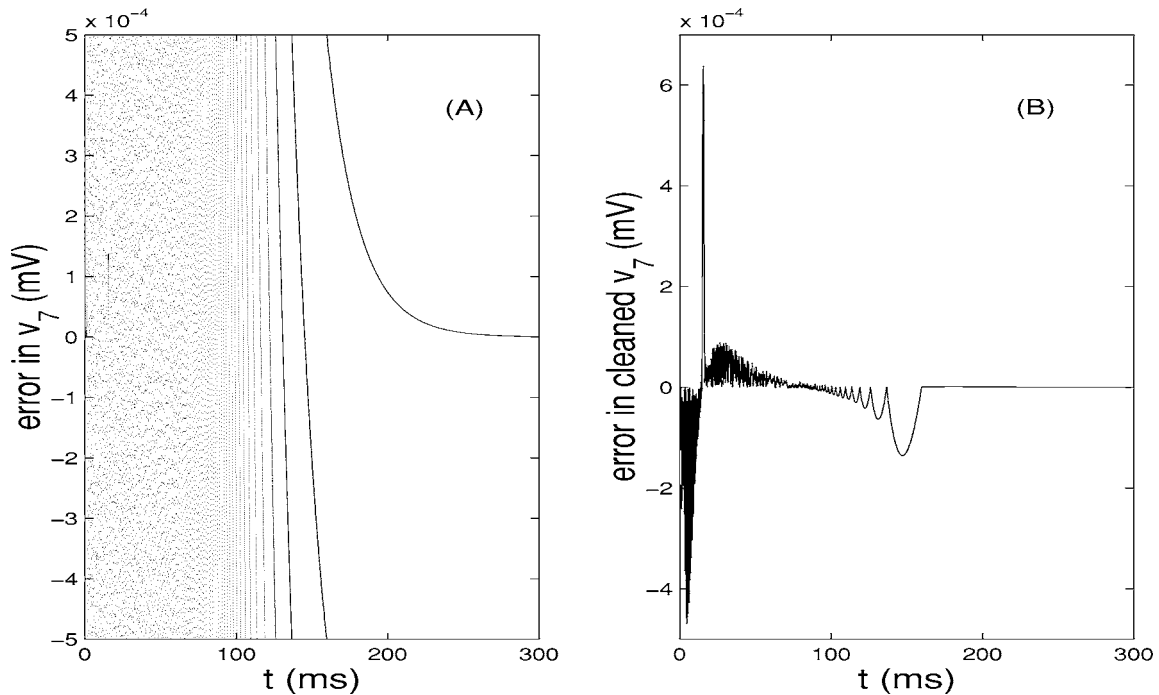


Figure 9. **A**: Difference between the true and measured signals, $v_7(\ell_7, t) - \tilde{v}_7(\ell_7, t)$. **B**: Difference between the true and cleaned measured signals, $v_7(\ell_7, t) - \text{clean}(\tilde{v}_7(\ell_7, t))$.

Table 8. True and recovered LDT parameters drawn from cleaned measurements and knowledge that $C_m = 1$. ($\Delta_A = 15$ and $\Delta_H = 50$)

	R_i	C_m	G_H	G_A	G_I	G_{sh}
True	0.4	1	0.04	0.15	0.02	0.19894
$d = 3$	0.40028	1.0000	0.02615	0.23174	0.01937	0.19848

Again, this is a significant improvement over Table 5. We naturally expect that combining these two approaches should lead to even greater accuracy in the face of noisy measurements. As an indication that such is the case we apply them simultaneously to data accurate to only three digits in Table 8.

Hence, three digits of accuracy in the potential recordings is sufficient to recover the passive parameters to high precision and the correct order of magnitude of the active conductances.

7. Conclusions

We have established that a handful of weighted integrals of time recordings of the potential at two locations in an active dendritic neuron suffice, in theory, to determine the neuron's quasi-active parameters. The theory succeeded thanks to the beautiful connections between moments of the measurements and derivatives of the transfer function of the linearized neuron. We demonstrated, albeit on synthetic data, that our recovery algorithm enjoys some insensitivity to errors in the actual recorded potentials. This together with our preliminary insights into choice of stimulus, placement of dendritic electrode, and filtering of noisy recordings argues that our technique may well be applicable to "real" experimental data. Regarding the placement of the dendritic electrode we note, following Cox (1998), that the somatic potential most likely determines all the parameters of interest. The sensitivity of the recovered parameters to noise in the measurements will of course decrease with the imposition of additional physiological constraints—for example, the knowledge of dendritic potential at one or more sites or *a priori* knowledge of the passive parameters. With the advent of voltage activated dyes it is now possible (see, e.g., Fromherz and Müller, 1994) to know the potential at every point in the neuron. This study constitutes but one approach to the effective use of simultaneous potential recordings.

Finally, let us remark on limitations and generalizations. We have developed the technique for neurons

sporting two types of voltage-gated ion channels. Our theory can encompass many more, at a cost. The cost is roughly one additional moment for each additional conductance. In practice, the higher the moment, the greater its sensitivity to noise and therefore the poorer the estimate of the sought after conductance. This, however, is assuming that one wishes to simultaneously determine all conductances in one single sweep. If one is free to selectively block or otherwise alter channels, then the remaining channel conductances may of course be estimated with fewer moments. Rather than generalizing to more channel types, one may instead focus on characterizing more than just a channel's maximal conductance. Cox and Ji (2001) present fixed-point methods for determining the full kinetics (time constant and equilibrium functionals) for a typical potassium channel from somatic potential recordings.

Our theory has also assumed uniform material properties. Contrary to a growing body of experimental data (Shen et al., 1999), we do not permit our quasi-active parameters to vary with distance from the soma. As such, our recovered parameters are, at best, spatial averages of the true distributions. Numerical experimentation has suggested to us that one or two potential recordings (following a subthreshold stimulus) are poor indicators of nonuniform conductances. This is in keeping with (see, e.g., Isakov, 1998) the ill-posed nature of the recovery of a spatial varying potential term from boundary measurements in a linear parabolic equation. We expect that the resolution of spatial non-homogeneties will have to exploit multiple recordings following suprathreshold stimulus.

Acknowledgement

This work was partially supported by NSF grant DMS-0077728.

References

- Agmon-Snir H (1995) A novel theoretical approach to the analysis of dendritic transients. *Biophys. J.* 69:1633–1656.
- Cox SJ (1998) A new method for extracting cable parameters from input impedance data. *Math. Biosci.* 153:1–12.
- Cox SJ, Ji L (2000) Identification of the cable parameters in the somatic shunt model. *Biol. Cybernetics* 83(2):151–159.
- Cox SJ, Ji L (2001) Discerning ionic currents and their kinetics from input impedance data. *Bulletin of Math. Bio.* 63(5):909–932.

- Fromherz P, Müller CO (1994) Cable properties of a straight neurite of a leech probed by a voltage-sensitive dye. *Proc. Natl. Acad. Sci. USA* 91:4604–4608.
- Isakov V (1998) *Inverse Problems for Partial Differential Equations*. Springer, New York.
- Johnston D, Magee JC, Colbert CM, Christie BR (1996) Active properties of neuronal dendrites. *Annual Review of Neuroscience* 19:165–186.
- Koch C (1999) *Biophysics of Computation*. Oxford University Press, Oxford.
- Mainen ZF, Sejnowski TJ (1998) Modeling active dendritic processes in pyramidal neurons. In: Koch C, Seger I, eds. *Methods in Neuronal Modeling* (2nd ed.). MIT Press, Cambridge, MA. pp. 171–210.
- Rall W, Burke RE, Holmes WR, Jack JJB, Redman SJ, Segev I (1992) Matching dendritic neuron models to experimental data. *Physiol. Rev.* 72:S159–S186.
- Shen GY, Chen WR, Midtgaard J, Shepherd GM, Hines ML (1999) Computational analysis of action potential initiation in mitral cell soma and dendrites based on dual patch recordings. *J. Neurophysiol.* 82:3006–3020.
- Surkis A, Peskin CS, Tranchina D, Leonard CS (1998) Recovery of cable properties through active and passive modeling of subthreshold membrane responses from laterodorsal tegmental neurons. *J. Neurophysiol.* 80(5):2593–2607.
- Vanier MC, Bower JM (1999) A comparative survey of automated parameter search methods for compartmental neural models. *J. of Comput. Neurosci.* 7(2):149–171.